AIAA 80-0269R

Nonlinear Supersonic Potential Flow over Delta Wings

B. Grossman* and M. J. Siclari†
Grumman Aerospace Corporation, Bethpage, N. Y.

A numerical procedure has been developed for the computation of the steady, inviscid supersonic flow over aircraft configurations. The technique accounts for major nonlinear effects (shock waves, blunt leading edges) at low to moderate supersonic speeds. A fully implicit marching technique for the full potential equation is utilized in a stereographically projected, conformally mapped, spherical coordinate frame. Cross-flow planes are efficiently solved by type-dependent relaxation techniques. Results are presented for several delta wing configurations and bodies of revolution, and are compared with existing experimental data, Euler's equations solutions, and results from linearized theories (panel methods).

I. Introduction

THE goal of the present investigation is the development of a highly efficient and general numerical procedure for the computation of the steady, inviscid supersonic flow over aircraft configurations. In particular, this paper will concentrate on the development and verification of the method through application to isolated delta wings and bodies of revolution. Emphasis will be given to the prediction of nonlinear effects at imbedded shock waves and blunt leading edges in the low to moderate supersonic Mach number range.

Existing computational techniques in this regime may be broadly characterized as panel methods and finite-difference methods. Panel methods, which have been demonstrated to be widely versatile and quite efficient, have reached a very advanced stage of development and utility for subsonic flows. Efforts are continuing to improve their capabilities at supersonic speeds (i.e., Ehlers et al.[1]). These methods address the solution to the first-order linear small-disturbance equation with various approximations for the boundary conditions.

Finite-difference techniques for wing planforms in the supersonic regime concentrate on solutions to Euler's equations with differing treatments of shock waves, shock capturing[2] or shock fitting,[3-5] and a variety of methods for grid generation (i.e., Moretti[5]) and geometry input. The major drawbacks of these methods are associated with their large computational times which are due primarily to the fine grids necessary to resolve thin wings and the accompanying strict stability requirements. Other problem areas for the Euler solutions in the Mach number range considered here are due to subsonic Mach numbers in the axial marching direction, initial conditions at the apex of the wing or body, and vortical singularities of the leeward surface.

In a recent paper by Mason and daForno[6] the opportunities for performance gains through nonlinear aerodynamic effects are discussed including the impact on nonlinear computational analysis and design. A convincing case is made for the necessity of the inclusion of nonlinear effects particularly for wing leading edges and imbedded shock waves for the aerodynamic design and analysis of wings.

In the transonic speed regime, finite-difference methods have made an impact on aerodynamic design. The mixed-flow relaxation techniques solving the transonic small-disturbance and full potential equation have been quite successful in developing nonlinear solutions to a variety of two- and three-dimensional configurations in a reasonable amount of computing time. The results degrade considerably at freestream Mach numbers greater than one.

An initial attempt on the rapid solution of nonlinear supersonic flow problems has been performed by the first author for the restricted case of conical flows.[7] This methodology utilized the similarity property of conical flows to reduce the problem to two dimensions and contained the assumption of irrotational flow. Although the entropy was neglected in the flowfield, accurate results were obtained provided the Mach number normal to all shock waves was less than ~ 1.4. For most practical swept wing configurations, this will be the case in the Mach number range $1.2 < M_\infty < 2.4$ considered here. An orthogonal coordinate system was developed based on a stereographic projection and conformal mapping methods, that was well suited to a variety of arbitrary smooth conical bodies including extremely thin elliptic cones. The governing potential-flow equation was shown to contain the salient mathematical features of the transonic full potential equation. A type-dependent relaxation procedure was developed for the mixed elliptic-hyperbolic flowfield in the conical cross-flow plane. The numerical solutions for a variety of geometries at moderate supersonic speeds over a range of incidences were compared to several other theoretical methods and experimental data. The agreement with experimental results was very good for conditions where the flow did not separate. Of particular importance was the very successful comparison between the conical potential solution and the more "exact" solutions by the method of lines and finite-difference solutions to Euler's equations with shock fitting. The excellent agreement, particularly for the strength and position of the shock waves, established the validity of the irrotational flow assumption for the moderate supersonic Mach number range. In a recent series of wind-tunnel experiments by Mason,[8] excellent comparisons with numerical solutions from the method in Ref. 7 are shown for the pressure distribution on two thin conical wings, a flat wing, and a conically cambered wing, at high values of lift coefficient and Mach numbers ranging from 1.6 to 2.0. The comparisons in Ref. 8 illustrate the importance of a nonlinear computational tool.

The methodology of the conical flow solutions serves as a starting point for the development of a computational technique for supersonic flows over general (nonconical) configurations. It is intended that this technique bridge the gap between panel methods and Euler's equations techniques

Presented as Paper 80-0269 at the AIAA 18th Aerospace Sciences Meeting, Pasadena, Calif., Jan. 14-16, 1980; submitted July 21, 1980; revision received Dec. 11, 1980.

*Laboratory Head, Theoretical Aerodynamics. Currently, Associate Professor, Department of Aerospace and Mechanical Engineering; Polytechnic Institute of N. Y., Farmingdale, N. Y. Member AIAA.

†Senior Research Scientist. Member AIAA.

by utilizing the irrotational flow approximation to simplify and accelerate the solution procedure and still retain important nonlinear effects.

The present technique consists of a hyperbolic marching procedure for the three-dimensional full potential equation. Solutions are obtained by marching along spherical radii and solving for the spherical cross-flow planes with a fully implicit type-dependent relaxation method. A complete description of the mapped coordinate system is given in Sec. II along with a procedure for geometry definition. The derivation of the governing equations and boundary conditions appears in Sec. III, followed by the numerical formulation in Sec. IV. Several solutions are then presented for delta wings and bodies of revolution, along with comparisons with Euler solutions, linearized methods, and experimental data.

II. Mappings and Grid Generation

Existing finite-difference supersonic marching techniques generally begin with a Cartesian coordinate frame x, y, z with the centerline of the geometry coincident with the z axis and marching downstream in z. This procedure has the drawback of requiring the axial Mach number to be greater than unity throughout the flowfield. This condition can be easily violated along the leading edge of the wing at low supersonic Mach numbers and practical sweep angles. This usually limits the applicability of the method to a condition where $M_\infty > 1.8 \sim 2.0$. This drawback can be eliminated with the utilization of a spherical coordinate frame ψ, ω, r where

$$x = r\cos\omega\sin\psi, \qquad y = r\sin\omega\sin\psi, \qquad z = r\cos\psi \tag{1}$$

with the centerline of the body along the r axis at $\psi = 0$. The numerical solution will be obtained by marching on spherical surfaces in the r direction. Hence, the leading edge of a constant sweep angle or delta wing will be coincident with the marching direction. To solve the exact potential flow equation with exact boundary conditions on relatively general wings, a transformed domain on each spherical surface must be generated where the mapped body surface is a coordinate line and with adequate mesh spacing in regions of steep flow gradients. In Ref. 7, a series of mappings were developed for conical bodies which meet these requirements. First a preliminary mapping, called a stereographic projection (i.e., Weatherburn[9]), is used to open the sphere $r = \text{const}$ to a planar surface by

$$p + iq = \tan(\psi/2)e^{i\omega} \tag{2}$$

Now, as discussed in Ref. 7, it is convenient to map the body cross section to a near circle by a Joukowski mapping

$$\frac{S - S_0}{S + \bar{S}_0} = \left(\frac{\Gamma - S_0/2}{\Gamma + \bar{S}_0/2}\right)^2 \tag{3}$$

where

$$S = p + iq \qquad \Gamma = \rho e^{i\theta} \tag{4}$$

and $S_0 = S_0(r)$ is the location of the singularity in the p, q plane.

The mapped domain, consisting of the curvilinear coordinates ρ, θ, and $R = r$ form the basis of the computation. The nonorthogonality of the coordinate system enters from the dependency of the singularity location on r, $S_0 = S_0(r)$. Thus, derivatives with respect to R (with ρ and θ const) generally differ from derivatives with respect to r (at constant ψ and ω). However, as will be noted in the next section, the coordinates ρ, θ are orthogonal with respect to each other at $R = \text{const}$. It is convenient to introduce here the two metric lengths for the orthogonal coordinates

$$h_\rho = \left[\left(\frac{\partial x}{\partial \rho}\right)^2 + \left(\frac{\partial y}{\partial \rho}\right)^2 + \left(\frac{\partial z}{\partial \rho}\right)^2\right]^{1/2} = RH(\rho,\theta,R)$$

$$h_\theta = \left[\left(\frac{\partial x}{\partial \theta}\right)^2 + \left(\frac{\partial y}{\partial \theta}\right)^2 + \left(\frac{\partial z}{\partial \theta}\right)^2\right]^{1/2} = \rho RH(\rho,\theta,R) \tag{5}$$

where

$$H = \sin\psi / [(p^2 + q^2)^{1/2}]h \tag{6}$$

with h being the metric of the conformal mapping at constant r

$$h = \left|\frac{\partial S}{\partial \Gamma}\right| = \left|\frac{(S - S_0)(S + \bar{S}_0)}{(\Gamma - S_0/2)(\Gamma + \bar{S}_0/2)}\right| \tag{7}$$

The derivative of the transformations in the r direction, denoted h_1 and h_2 are given by

$$h_1(\rho,\theta,R) \equiv \frac{\partial \rho}{\partial r} = \xi\cos\theta + \eta\sin\theta$$

$$h_2(\rho,\theta,R) \equiv \frac{1}{\rho}\frac{\partial \theta}{\partial r} = \xi\sin\theta - \eta\cos\theta \tag{8}$$

where

$$\xi + i\eta \equiv \frac{\partial S}{\partial r} \Big/ \frac{\partial S}{\partial \Gamma}$$

The numerical computation will be performed in a sheared coordinate system defined by

$$X = \theta \qquad Y = \frac{\rho - b(\theta,R)}{c(\theta,R) - b(\theta,R)} \qquad Z = R \tag{9}$$

where $b(\theta,R)$ is the mapped body surface coordinate (near circle) and $c(\theta,R)$ is a somewhat arbitrary predefined smooth surface located outside the bow wave.

The wing geometry input utilizes conventional chordwise data to model the wing. This data is curve fit using bicubic surface patches[10] as described in Ref. 11. Unlike methods that model wings using flat panels for linearized panel-method codes, this technique defines the wing with nonlinear surface panels satisfying first derivative continuity requirements at the panel boundaries. Surface geometry is then developed along spherical surface grid points in the mapped domain to define the function $b(\theta,R)$.

III. Governing Equations and Boundary Conditions

For inviscid flow, the governing steady flow equations in terms of the velocity vector $\bar{Q}$ and the speed of sound a may be written as

$$a^2 \nabla \cdot \bar{Q} - \tfrac{1}{2}\bar{Q} \cdot \nabla(\bar{Q} \cdot \bar{Q}) = 0 \tag{10}$$

and

$$a^2 + [(\gamma - 1)/2]\bar{Q} \cdot \bar{Q} = a_0^2 \tag{11}$$

where a_0 is the stagnation speed of sound and γ the ratio of specific heats. A perturbation potential ϕ is introduced such that

$$\bar{Q} = \bar{q} + \bar{q}_\infty = \nabla\phi + \bar{q}_\infty \tag{12}$$

where the freestream velocity vector at angle of attack α may be written in the original Cartesian coordinates as

$$\bar{q}_\infty = \sin\alpha\,\hat{j} + \cos\alpha\,\hat{k} \tag{13}$$

In order that the potential ϕ reduce to the conical flow potential F as defined in Ref. 7, let

$$\phi = RF(\rho,\theta,R) \tag{14}$$

where for conical flows F will only depend upon ρ and θ.

The transformation of the governing Eqs. (10) and (11) in the nonorthogonal coordinate system ρ, θ, R through Eqs. (1-8) is quite tedious. A convenient device for handling the algebra develops from the fact that the ρ and θ coordinates are mutually orthogonal along surfaces $R = \text{const}$. This derivation follows a technique used by Moretti[12] for a nonorthogonal, mapped Cartesian coordinate system. The procedure basically consists of first transforming the vector operations in Eq. (10) to spherical coordinates using standard orthogonality rules. Then the cross-flow terms (ψ, ω) are further transformed to the (ρ, θ) coordinates using the appropriate two-dimensional orthogonality relationships. The remaining r derivatives are then transformed separately. The procedure is simplified by considering the mixed velocity vector

$$\bar{Q} = V\,\hat{i}_\rho + U\,\hat{i}_\theta + W\,\hat{i}_r \tag{15}$$

Note that in general $\hat{i}_r$ will have components in the $\hat{i}_\rho$, $\hat{i}_\theta$, and $\hat{i}_R$ directions. Following this prescription we have

$$\nabla\phi = \nabla_c\phi + \frac{\partial\phi}{\partial r}\,\hat{i}_r = v\,\hat{i}_\rho + u\,\hat{i}_\theta + w\,\hat{i}_r \tag{16}$$

where

$$\nabla_c\phi = \frac{1}{RH}\frac{\partial\phi}{\partial\rho}\,\hat{i}_\rho + \frac{1}{\rho RH}\frac{\partial\phi}{\partial\theta}\,\hat{i}_\theta \tag{17}$$

The notation ∇_c refers to the "cross-flow" gradient that can be shown to follow the transformation properties of a two-dimensional orthogonal coordinate system.

Introducing the definition Eq. (14) into Eqs. (16), (17), and (12), the velocity components are obtained as

$$V = v + v_\infty = \frac{1}{H}\frac{\partial F}{\partial\rho} + v_\infty(\rho,\theta,R)$$

$$U = u + u_\infty = \frac{1}{\rho H}\frac{\partial F}{\partial\theta} + u_\infty(\rho,\theta,R)$$

$$W = w + w_\infty = F + R\frac{\partial F}{\partial r} + w_\infty(\rho,\theta,R) \tag{18}$$

where

$$v_\infty = \frac{1}{H}\left[\sin\alpha\left(\cos\psi\sin\omega\psi_\rho - \cos\omega\frac{1}{\rho}\psi_\theta\right) - \cos\alpha\sin\psi\psi_\rho\right]$$

$$u_\infty = \frac{1}{H}\left[\sin\alpha\left(\cos\omega\psi_\rho + \cos\psi\sin\omega\frac{1}{\rho}\psi_\theta\right) - \cos\alpha\sin\psi\frac{1}{\rho}\psi_\theta\right]$$

$$w_\infty = \sin\alpha\sin\psi\sin\omega + \cos\alpha\cos\psi \tag{19}$$

and ψ, ω are related to ρ, θ, R through Eqs. (1-7).

Considering the first term in the governing equation (10), introducing Eq. (12), and noting that $\bar{q}_\infty$ is a constant vector, then

$$\nabla\cdot\bar{Q} = \nabla\cdot\bar{q} = \nabla_c\cdot\bar{q} + \frac{1}{r^2}\frac{\partial}{\partial r}(r^2 w) \tag{20}$$

Similarly, the second term of Eq. (10) becomes

$$\bar{Q}\cdot\nabla(\bar{Q}\cdot\bar{Q}) = \bar{Q}\cdot[\nabla(\bar{q}\cdot\bar{q}) + 2\nabla(\bar{q}_\infty\cdot\bar{q})] \tag{21}$$

where

$$\bar{Q}\cdot\nabla(\bar{q}\cdot\bar{q}) = \bar{Q}\cdot\nabla_c(\bar{q}\cdot\bar{q}) + W\frac{\partial}{\partial r}(\bar{q}\cdot\bar{q}) \tag{22}$$

and utilizing irrotationality conditions

$$\bar{Q}\cdot\nabla(\bar{q}_\infty\cdot\bar{q}) = \bar{Q}\cdot(\bar{q}_\infty\cdot\nabla)\bar{q} = \bar{Q}\cdot\left[\bar{q}_\infty\cdot\nabla_c + w_\infty\frac{\partial}{\partial r}\right]\bar{q} \tag{23}$$

The last term of Eq. (23) can be developed through direct transformation of Eqs. (1-8) as

$$\frac{\partial\bar{q}}{\partial r} = \left[\frac{\partial v}{\partial r} - \frac{u}{\rho}\frac{\partial}{\partial\theta}\left(\frac{\partial\rho}{\partial r}\right)\right]\hat{i}_\rho + \left[\frac{\partial u}{\partial r} + \frac{v}{\rho}\frac{\partial}{\partial\theta}\left(\frac{\partial\rho}{\partial r}\right)\right]\hat{i}_\theta + \frac{\partial w}{\partial r}\,\hat{i}_r \tag{24}$$

The only terms remaining to be transformed involve the r derivatives. Noting that

$$\frac{\partial}{\partial r} = \frac{\partial}{\partial R} + \frac{\partial\rho}{\partial r}\frac{\partial}{\partial\rho} + \frac{\partial\theta}{\partial r}\frac{\partial}{\partial\theta} \equiv \frac{\partial}{\partial R} + h_1\frac{\partial}{\partial\rho} + \frac{1}{\rho}h_2\frac{\partial}{\partial\theta} \tag{25}$$

where $h_1 = h_1(\rho,\theta,R)$ and $h_2 = h_2(\rho,\theta,R)$ are defined in Eq. (8). Substituting the expressions Eqs. (14-25) into the governing Eqs. (10) and (11) and performing a number of algebraic manipulations yields the following governing equations:

$$(a^2 - V^2)\frac{\partial^2 F}{\partial\rho^2} - 2UV\left(\frac{1}{\rho}\frac{\partial^2 F}{\partial\rho\partial\theta} - \frac{1}{\rho^2}\frac{\partial F}{\partial\theta}\right) + (a^2 - U^2)\left(\frac{1}{\rho^2}\frac{\partial^2 F}{\partial\theta^2} + \frac{1}{\rho}\frac{\partial F}{\partial\rho}\right) + (V^2 - U^2)\left(v\frac{\partial H}{\partial\rho} - \frac{u}{\rho}\frac{\partial H}{\partial\theta}\right) + 2UV\left(u\frac{\partial H}{\partial\rho} + \frac{v}{\rho}\frac{\partial H}{\partial\theta}\right) + H^2 w(2a^2 - V^2 - U^2)$$
$$= RH[(W^2 - a^2)RHh_1 + 2WV]\left[h_1\frac{\partial^2 F}{\partial\rho^2} + \frac{h_2}{\rho}\frac{\partial^2 F}{\partial\rho\partial\theta} + \frac{\partial^2 F}{\partial\rho\partial R} + H\left(v\frac{\partial h_1}{\partial\rho} + u\frac{\partial h_2}{\partial\rho} - \frac{u}{\rho}h_2\right)\right] + \frac{1}{\rho}RH[(W^2 - a^2)RHh_2 + 2WU] \times\left[h_1\frac{\partial^2 F}{\partial\rho\partial\theta} + \frac{h_2}{\rho}\frac{\partial^2 F}{\partial\theta^2} + \frac{\partial^2 F}{\partial\theta\partial R} + H\left(v\frac{\partial h_1}{\partial\theta} + u\frac{\partial h_2}{\partial\theta}\right)\right]$$

$$+RH^2(W^2-a^2)\left[R\left(h_1\frac{\partial^2F}{\partial\rho\partial R}+\frac{h_2}{\rho}\frac{\partial^2F}{\partial\theta\partial R}+\frac{\partial^2F}{\partial R^2}\right)\right.$$

$$\left.+2\frac{\partial F}{\partial R}+2H(vh_1+uh_2)+RH\left(v\frac{\partial h_1}{\partial R}+u\frac{\partial h_2}{\partial R}\right)\right] \quad (26)$$

and

$$a^2+[(\gamma-1)/2](V^2+U^2+W^2)=a_0^2 \quad (27)$$

The preceding equations, although appearing somewhat formidable are actually in a significantly simpler form than the general nonorthogonal second-order potential equation which contains 27 first and second derivative transformation terms. For conical flows, all R derivatives vanish and, hence, the right-hand side of Eq. (26) goes to zero, leaving the identical equation developed in Ref. 7. This feature enables an initial starting solution for the marching procedure to be developed from a conical flow. The mixed elliptic-hyperbolic nature of the cross-flow (U, V) plane is apparent in the left-hand side of Eq. (26) and the similarity to the two-dimensional transonic full potential equation may be noted. The equations will be hyperbolic in the R direction and solutions may be obtained by marching provided W, the velocity in the r direction is greater than the speed of sound, as seen from the coefficient of the F_{RR} term.

The governing equation in the final computational domain is obtained through the shearing transformation Eqs. (9),

$$(A_1-B_1)F_{XX}+(A_2-B_2)F_{XY}+(A_3-B_3)F_{YY}$$
$$+(A_4-B_4)F_Y+A_5F_X+A_6w+(A_7-B_7)$$
$$=B_8F_{ZZ}+B_9F_{XZ}+B_{10}F_{YZ}+B_{11}F_Z \quad (28)$$

where the coefficients A_i are identical to the conical terms in Ref. 7. The nonconical terms B_i are seen to be

$$B_1=\frac{C_2h_2}{\rho^2}$$

$$B_2=\frac{1}{\rho}(C_1h_2Y_\rho+2C_2h_2Y_\theta+C_2Y_R+C_3Rh_2Y_R+C_2h_1Y_\rho)$$

$$B_3=C_1h_1Y_\rho^2+\frac{Y_\theta}{\rho}\left(\frac{C_2h_2Y_\theta}{\rho}+C_1h_2Y_\rho+C_2h_1Y_\rho+C_2Y_R\right)+C_1Y_\rho Y_R+C_3RY_R\left(\frac{h_2Y_\theta}{\rho}+h_1Y_\rho+Y_R\right)$$

$$B_4=C_1\left(h_1Y_{\rho\rho}+\frac{h_2}{\rho}Y_{\rho\theta}+Y_{\rho R}\right)+\frac{C_2}{\rho}\left(\frac{h_2}{\rho}Y_{\theta\theta}+Y_{\theta R}+h_1Y_{\rho\theta}\right)+C_3R\left(h_1Y_{\rho R}+\frac{h_2}{\rho}Y_{\theta R}+Y_{RR}+\frac{2Y_R}{R}\right)$$

$$B_7=C_1H\left(vh_{1\rho}+uh_{2\rho}-\frac{uh_2}{\rho}\right)+\frac{C_2H}{\rho}(vh_{1\theta}+uh_{2\theta})+C_3H[2(uh_2+vh_1)+R(uh_{2R}+vh_{1R})]$$

$$B_8=C_3R$$

$$B_9=\frac{C_2}{\rho}+\frac{C_3Rh_2}{\rho}$$

$$B_{10}=\frac{C_2Y_\theta}{\rho}+\frac{C_3Rh_2Y_\theta}{\rho}+C_1Y_\rho+C_3R(h_1Y_\rho+2Y_R)$$

$$B_{11}=2C_3$$

where

$$C_1\equiv RH[(W^2-a^2)RHh_1+2WV]$$

$$C_2\equiv RH[(W^2-a^2)RHh_2+2WU]$$

$$C_3\equiv RH^2(W^2-a^2)$$

The boundary condition at the body surface is zero normal velocity. In terms of the mapped coordinates this condition implies at $\rho=b(\theta, R)$

$$bV-b_\theta U+bRH[h_1-(h_2b_\theta/b)-b_R]W=0$$

Utilizing the shearing transformation, Eq. (9), and Eqs. (18) to obtain

$$\left(\frac{\partial F}{\partial Y}\right)_{Y=0}=(c-b)[b_\theta F_X+bH(b_\theta u_\infty-bv_\infty)$$
$$-RH^2\lambda(bF+bRF_Z+h_2RF_X+bw_\infty)]/(b^2+b_\theta^2+R^2H^2\lambda^2) \quad (29)$$

where

$$\lambda\equiv bh_1-h_2b_\theta-bb_R$$

In the far field, outside the bow wave, the perturbation potential and its first derivatives must vanish

$$F,\frac{\partial F}{\partial X},\frac{\partial F}{\partial Y},\frac{\partial F}{\partial Z}\to 0 \text{ outside the bow wave} \quad (30)$$

The implementation of the far-field boundary condition will be discussed in the next section.

IV. Numerical Formulation

The numerical solution of the governing three-dimensional full potential Eq. (28) subject to boundary conditions Eqs. (29) and (30) is developed through a hyperbolic marching procedure in the Z (mapped spherical radius) direction as shown in Fig. 1. First-order backward differences are used to approximate all Z derivatives of the potential F, on the right-hand side of Eq. (28). Thus, if the indices i, j, k are used to depict the location in the x, y, z directions, respectively, of the grid point where the solution is to be evaluated, then a typical derivative becomes

$$(F_{ZZ})_{i,j,k}=(F_{i,j,k}-2F_{i,j,k-1}+F_{i,j,k-2})/\Delta Z^2$$

The values $F_{i,j,k-1}$ and $F_{i,j,k-2}$ are known from the solution at previous stages of the marching calculation or from initial starting conditions. The cross-flow terms (X, Y) on the left-hand side of Eq. (28) are all evaluated at the present values of $Z=k\Delta Z$. Thus, a fully implicit, coupled set of finite-difference equations is obtained for the perturbation potential F at all values of the cross-flow plane (i, j) at the present kth Z station. This particular formulation of the marching procedure was suggested in discussions with South[13] and has the advantage of retaining the successful conical-flow

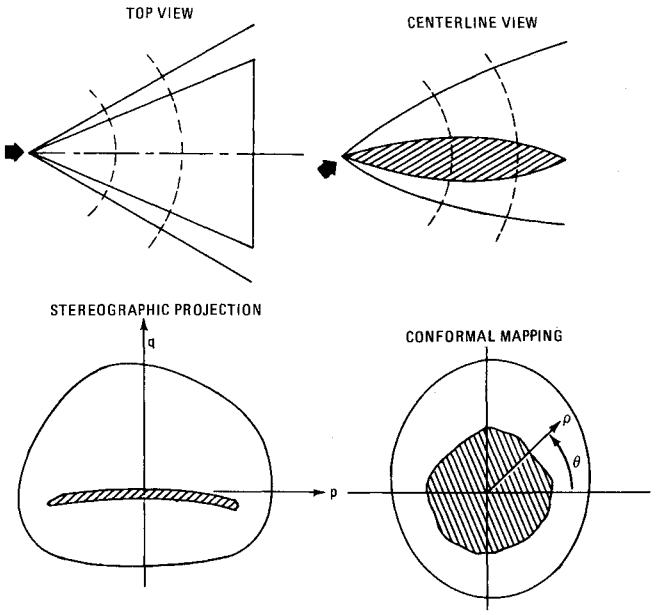

Fig. 1 Schematic of the marching procedure including mapped cross sections.

relaxation procedure of Ref. 7 with the Z derivatives acting as forcing functions. Furthermore, since the cross-flow difference equations are fully implicit, the radial step size ΔZ will not be subject to any stability limitations.

The cross-flow solution is determined using type-dependent relaxation techniques similar to those developed by Jameson[14] for the transonic full potential equation. The nonconservative procedure used here is identical to the conical flow method, fully described in Ref. 7. The flow is integrated from a ring $Y=$const outside the bow wave toward the body using successive line over-relaxation and a rotated difference formulation. The cross-flow relaxation process was shown to very accurately capture the bow wave and wing imbedded shocks for conical flows.[7] In the present three-dimensional applications, the cross-flow plane $Z=$const will not, in general, be normal to the bow and imbedded shocks, and the rotated difference scheme will not be as effective in capturing shock waves as they become more oblique to the grid. This will result in oblique shocks being spread over slightly more mesh points than for normal shocks. However, for the applications considered here, i.e., delta wings and bodies of revolution, the coordinate system in the present formulation will produce shocks with adequate resolution.

As previously discussed, two complete cross-flow solutions for the potential function F are needed to initiate the marching solution. If the geometry begins from a conical body, the starting solutions are determined from the governing Eqs. (27) and (28) with all the Z (or R) derivatives set to zero. The right-hand side of Eq. (28) then vanishes and the conical solution is found, as described in Ref. 7. For nonconical initial geometries, a very small conical "nose" is assumed to exist and conical initial conditions are again utilized. This procedure should be more accurate than the more approximate and often time consuming methods used for the initialization of Euler's equations solutions (e.g., Ref. 3).

The basic numerical procedure outlined here might appear to be quite inefficient since the marching solution requires the complete convergence of a relaxation method at each Z station, a step usually requiring several hundred iterations for conical flows. However, it has been found for the applications considered here, that each cross-flow station does not vary substantially from the previous one, and except for the initial conical solution, the remaining cross-flow solutions usually converge in 20-40 iterations. Specific details of the convergence histories will be given in the next section.

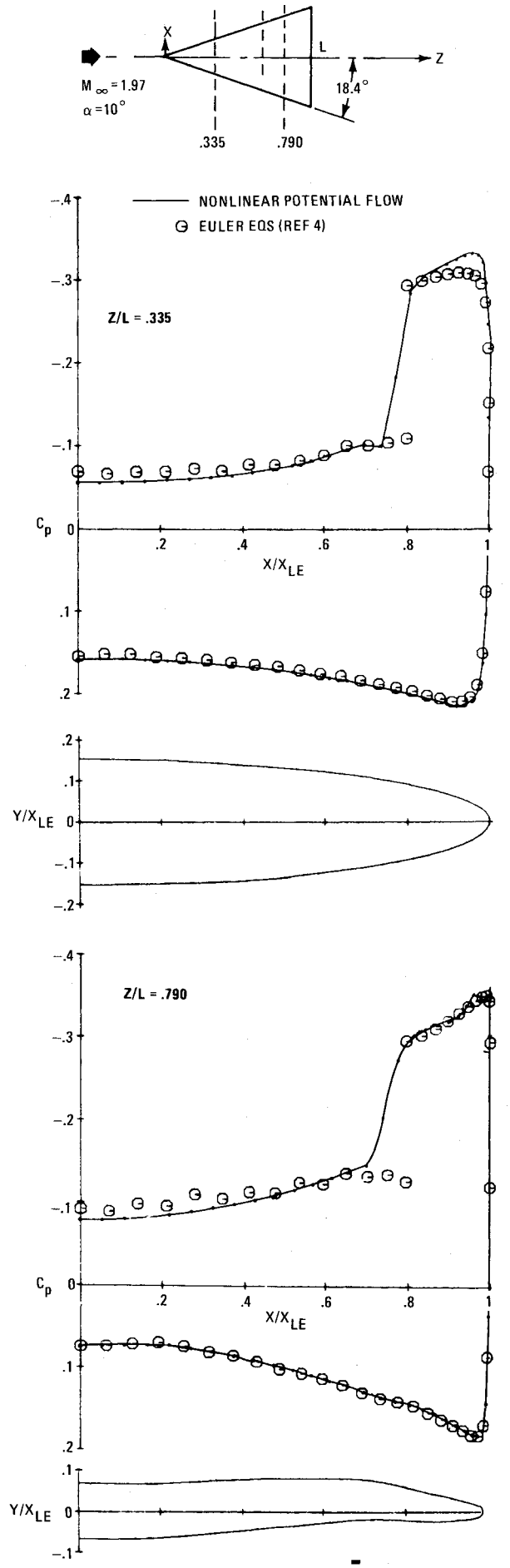

Fig. 2 Comparison with Euler's equations solution for an initially conical delta wing.

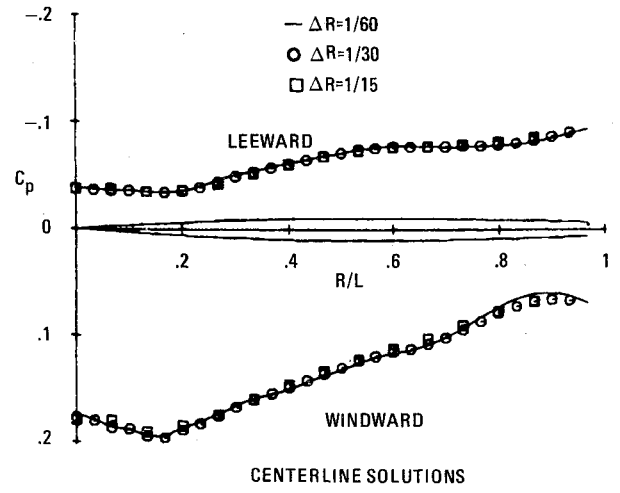

Fig. 3 Effect of mesh spacing in the marching direction for a delta wing.

V. Results and Discussion

As a first comparison, the flow over an initially conical delta wing, previously computed using an Euler's equations method with shock fitting,[4] is considered. Figure 2 shows a comparison of the surface pressure distributions for two vertical transverse planes at $M_\infty = 1.97$ and $\alpha = 10$ deg with a wing planform angle of 18.39 deg (corresponding to a sweepback angle $\Lambda = 71.61$ deg). The geometry of the delta wing contains both thickness and camber variation. The nonlinear potential flow solution shows excellent agreement with the Euler solution including the important nonlinear effects near the leading edge and the imbedded shock wave. Of particular importance is the excellent agreement in the strength and position of the imbedded shock wave (although the potential solution is spread over several mesh intervals), which serves to confirm the validity of the irrotational flow assumption. The potential flow solution was generated using a mesh of 60×60 in the cross-flow plane with 60 steps in the radial marching direction and required 15-30 iterations at each cross-flow station. The Euler solution using an explicit marching technique typically takes the order of several thousand axial steps due to restrictions on step size required by the CFL stability criterion. For even thinner wings, with smaller radii of curvature at the wing leading edge and correspondingly finer mesh resolution, the Euler solutions will require even more axial steps. The present method, as discussed in Sec. IV, does not have this requirement.

To illustrate the dependence of the accuracy of the present method on the radial (marching) step size, the solution of the delta wing in Fig. 2 was repeated using 60, 30, and 15 marching steps. Figure 3 presents the step size comparison for the windward and leeward symmetry plane pressure distributions. The dependency on step size is seen to be minimal. Obviously, if the geometry of the wing changed more rapidly or abruptly, finer marching grids would become necessary.

The next two series of results indicate the ability of the present technique to handle the stringent geometrical requirements of practical supersonic delta wings. Solutions are obtained for delta wings with a basic NACA 65A003 airfoil section (maximum thickness only 3%), and a 70 deg sweepback, for which there is available wind-tunnel surface pressure data.[15] Figure 4 shows a correlation of the chordwise pressure distribution between the nonlinear potential flow solution and the test data for the delta wing at $M_\infty = 2.01$ and $\alpha = 6$ deg.

On the windward surface the agreement with the data is good on the three span stations shown in Figs. 4a-c. The correlation on the leeward surface degrades drastically on the outboard stations. This is likely due to viscous effects causing shock-induced boundary-layer separation. Also shown on

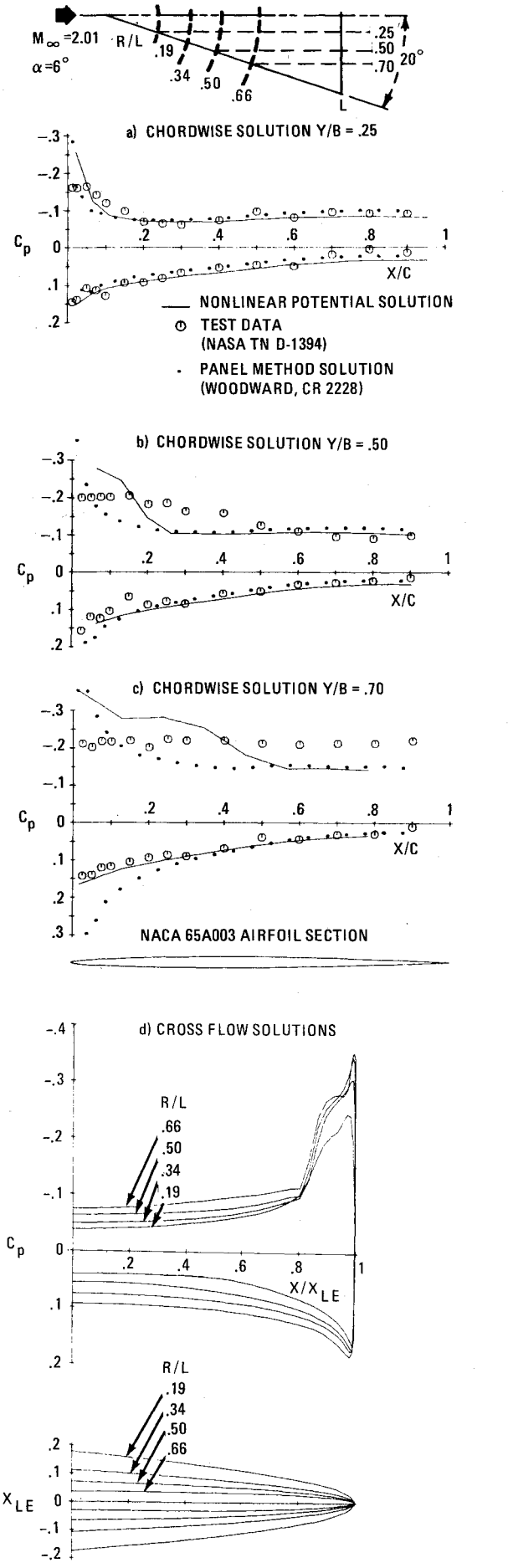

Fig. 4 Comparison with test data and panel method solution for a flat delta wing at $\alpha = 6$ deg.

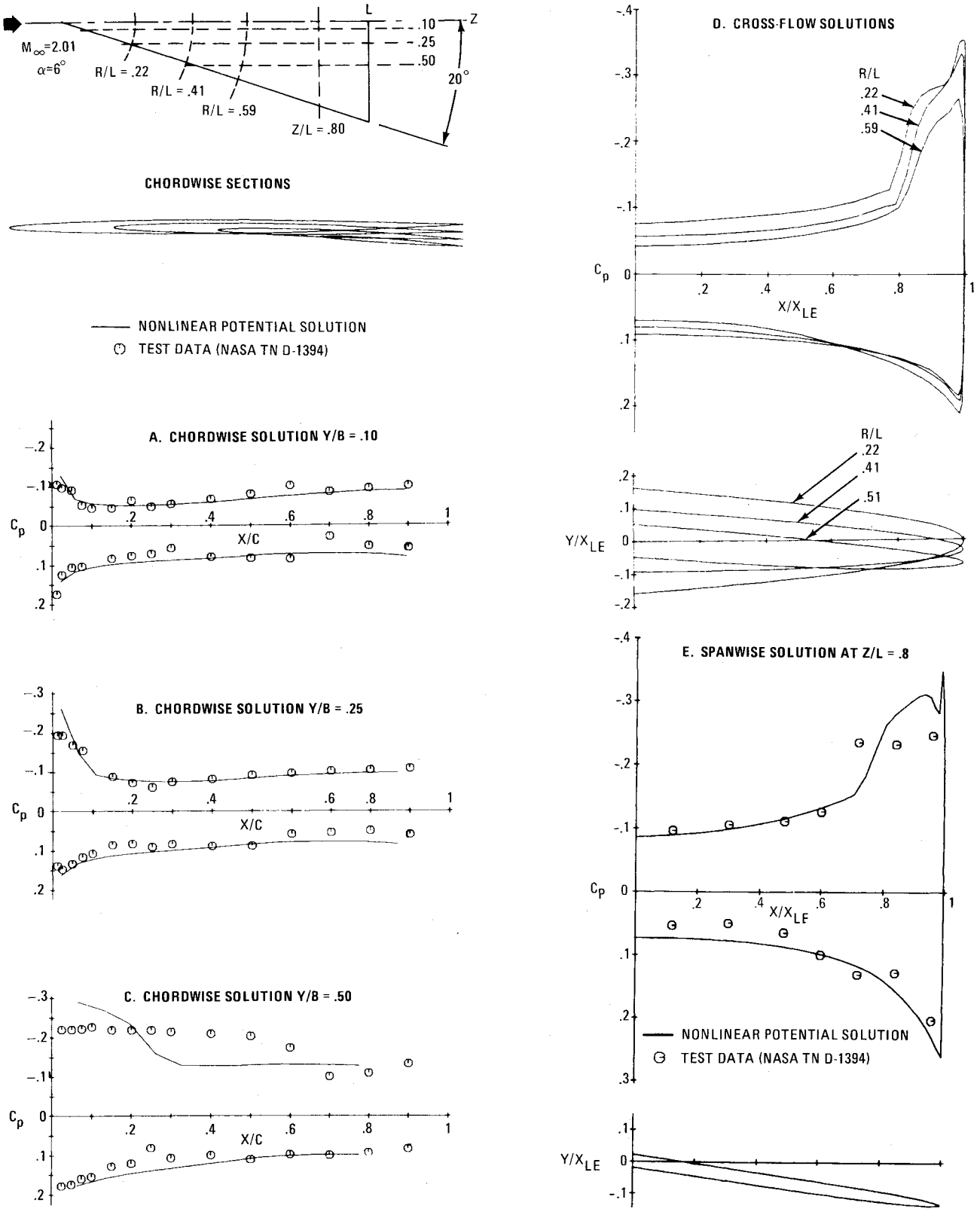

Fig. 5 Comparison with experimental data for a cambered and twisted delta wing.

these plots are panel method solutions.[16] As expected, the linearized solution does not correlate well near the leading edge, particularly evident in the most outboard span station, and precludes imbedded shock wave effects. Unfortunately, the apparent flow separation on the leeward surface reduces the impact of the comparison of the two solutions with the test data. The imbedded shock wave in the nonlinear potential solution appears to be very crudely resolved in the chordwise pressure distributions. This results from the linear interpolations of the spherical cross-flow solutions (of which 32 marching steps were used for the computations in Fig. 4) and is amplified by the wing sweepback. In Fig. 4d, an overlay of several cross-flow pressure distributions is shown, with correspondingly better shock wave resolution. The location of the imbedded shock waves is apparently established very quickly and further changes in the thickness distribution does not significantly alter its location.

Figure 5 presents the nonlinear potential flow solution at $M_\infty = 2.01$, $\alpha = 6$ deg for another delta wing tested in Ref. 15. This wing has the same NACA 65A003 thickness distribution

as the preceding case, but with camber and twist off the centerline of the wing. Good correlation with the test data in the chordwise direction is again shown for the inboard span stations in Figs. 5a and b. At the 0.5 span station, Fig. 5c appears to indicate separated flow in the data on the leeward surface, with good agreement shown for the windward pressures. Several spherical spanwise pressure distributions are shown in Fig. 5d. The camber and twist of the wing apparently has a more pronounced effect on the position of the imbedded shock wave than the thickness effect shown previously in Fig. 4d. A comparison of the spanwise surface pressure distribution with the data is shown in Fig. 5e in a transverse plane corresponding to a station $Z/L = 0.80$. The test data points, and also the numerical solution were obtained in this plane by linear interpolation. Generally, good agreement was achieved in this plane with a scatter in the test data, probably enhanced by the interpolation of the relatively sparse data values. The lower pressures observed for the computed result in the supercritical region upstream of the imbedded shock are consistent with the leeward separated flow supposition. Suprisingly, relatively good agreement is shown in Fig. 5e for the shock location. Apparently, a small variation in shock location in the spanwise, transverse plane will be magnified when viewed along the chordwise direction, as shown in Figs. 5a-c.

The results shown in Figs. 4 and 5 indicate that it is quite difficult to correlate inviscid supersonic flow solutions with high-lift test data on thin delta wings especially at flow angles sufficient to generate supersonic cross flow and imbedded shocks that will inevitably cause leeward flow separation. This phenomena was also mentioned with respect to conical flows in Ref. 7. Most design procedures used previously for supersonic wings relied heavily on linearized theories that could not provide any information on imbedded shock waves. This design drawback for conditions of supersonic cross flow is discussed by Mason and daForno.[6] Recently, a high-lift wing was designed and tested[8] using the nonlinear potential theory for conical flows.[7] The wind-tunnel data verified the theoretical prediction of the optimistic high-lift design goal with virtually no separation at the design point due to a theoretically controlled imbedded shock strength.

Thus far, solutions have only been presented for geometries which have one spatial coordinate nearly coincident with a conical ray, i.e., the leading edge of delta wings. To further test the nonconical capability of the method, solutions were generated for several bodies of revolution. Excellent results with the present method have been obtained for Sears-Haack and Haack-Adams bodies of revolution as presented in Ref. 17.

The last set of results are for a circular-arc ogive cylinder for which wind-tunnel data has been presented in Ref. 18. Presented in Fig. 6 is the nonlinear potential solution compared with test data, an Euler's equation solution,[19] and two linearized solutions. One linearized solution used a panel method[16] with 30 axial sets of panels and the second utilized the superposition of approximately 70 axial conical flow singularities to satisfy the exact boundary conditions. Near the nose of the body, the linearized solutions differ significantly from the test data. Both the nonlinear potential solution and the Euler solution are in excellent agreement with each other and in fair agreement with the experimental data. The largest discrepancy occurs aft of the shoulder region which may possibly be due to boundary layer build up. Results for the same body at an angle of attack of 4 deg are shown in Fig. 7. The centerline leeward and windward surface pressure distributions are presented for the panel method, Euler solution, and the nonlinear potential flow method. The present results and the Euler solution are in excellent agreement for the leeward pressures and differ slightly for the windward pressure distributions. Both of these methods are in fair agreement with test data with the largest discrepancy again occurring aft of the shoulder region. The panel method

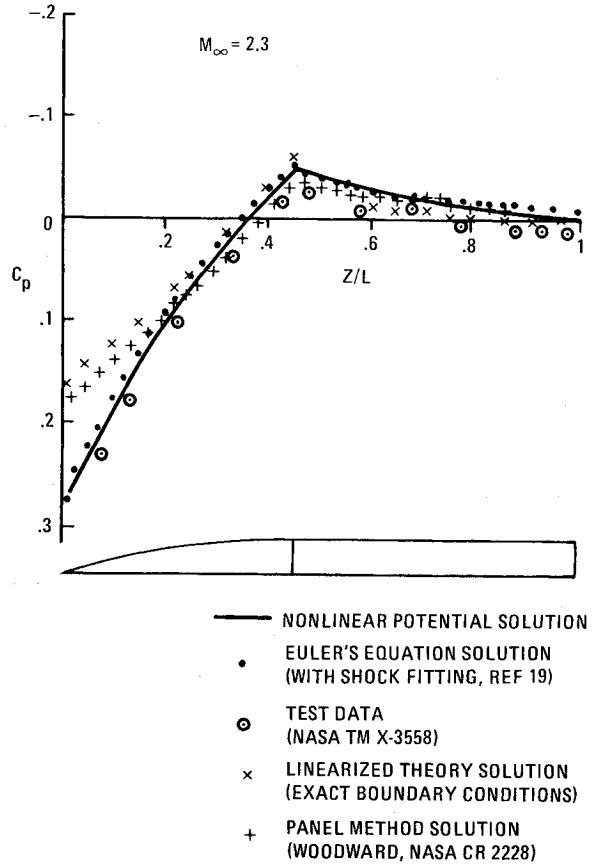

Fig. 6 Surface pressure distribution for a circular-arc cylinder body at $\alpha = 0$ deg.

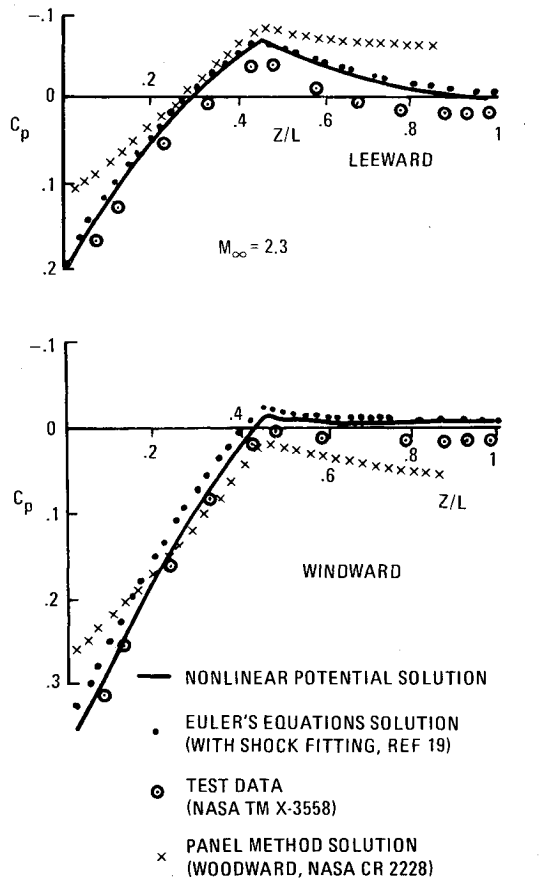

Fig. 7 Windward and leeward surface pressure distribution for a circular-arc cylinder body at $\alpha = 4$ deg.

solution is in poor agreement near the nose of the body and also exhibits unusual behavior aft of the shoulder region where the pressures do not tend to regain ambient conditions.

The numerical results for the nonlinear potential flow method were all run on an IBM 370/168 computer. The delta wing solutions typically utilized a cross-flow grid of 60×60 and used between 15 and 60 radial marching steps. After an initial conical solution requiring 200-300 relaxation iterations, the remaining radial stations converged in 20-40 iterations. This translates to total computer run times varying between 25 to 45 min. The body of revolution cases generally used a cross-flow grid of 30×30 with between 25-100 radial steps and a corresponding run time of 4-10 min. These computer times are generally several times faster than Euler solutions with corresponding cross-flow resolution and geometric complexity. In addition, prospects appear to be excellent to significantly reduce these computational times for the present method. In an as yet unpublished work, the first author has developed an approximate factorization (AF) algorithm for the conical-flow relaxation solution which has been found to reduce the computational time by at least a factor of 5. This method should be readily adaptable to the present solution procedure. Also, work is in progress to extend the nonlinear potential flow method to more complex geometric configurations including arrow wings and wing-body combinations.

Acknowledgments

This investigation was partially supported by the USAF Flight Dynamics Laboratory under Contract F33615-77-C-3126. The authors gratefully acknowledge the continued support of Drs. G. daForno and W. Mason of the Engineering Department and the helpful discussions with Drs. R. E. Melnik and F. Marconi of the Research Department.

References

[1] Ehlers, F. E., Epton, M. A., Johnson, F. T., and Rubbert, P. E., "An Improved Higher-Order Panel Method for Linearized Supersonic Flow," AIAA Paper 78-15, Jan. 1978.

[2] Kutler, P., "Computation of Three-Dimensional Inviscid Supersonic Flows," *Progress in Numerical Fluid Dynamics, Lecture Notes in Physics,* Vol. 41, Springer-Verlag, Berlin, 1975, pp. 287-374.

[3] Marconi, F. and Siclari, M. J., "A Study of the Inviscid Flow about Conically Cambered Delta Wings," AIAA Paper 78-58, Jan. 1978.

[4] Siclari, M. J., "Investigation of Cross Flow Shocks on Delta Wings in Supersonic Flow," *AIAA Journal,* Vol. 18, Jan. 1980, pp.85-93.

[5] Moretti, G., "Conformal Mappings for the Computation of Steady Three-Dimensional Supersonic Flows," *Numerical/Laboratory Computer Methods in Fluid Mechanics*, edited by A. A. Pouring and V. I. Shah, ASME, N.Y., 1979, pp. 13-28.

[6] Mason, W. H. and daForno, G., "Opportunities for Supersonic Performance Gains Through Non-Linear Aerodynamics," AIAA Paper 79-1527, July 1979.

[7] Grossman, B., "Numerical Procedure for the Computation of Irrotational Conical Flows," *AIAA Journal,* Vol. 17, Aug. 1979, pp. 828-837.

[8] Mason, W. H. and Miller, D. S., "Controlled Supercritical Crossflow on Supersonic Wings—An Experimental Validation," AIAA Paper 80-1421, July 1980.

[9] Weatherburn, C. E., *Differential Geometry of Three Dimensions,* Vol. I, University Press, Cambridge, England, 1955, pp. 167-173.

[10] Craidon, C. B., "A Computer Program for Fitting Smooth Surfaces to an Aircraft Configuration and Other Three-Dimensional Geometries," NASA TMX 3206, June 1975.

[11] Coons, S. A., "Surfaces for Computer-Aided Design of Space Forms," MAC-TR-41, Mass. Inst. of Tech., June 1967.

[12] Moretti, G., "Calculation of the Three-Dimensional Supersonic Inviscid Steady Flow Past an Arrow-Winged Airframe, Part I," Polytechnic Inst. of N. Y., POLY AE/AM Rept. 76-8, May 1976.

[13] South, J. C., private communication, NASA Langley Research Center, Hampton, Va., 1978.

[14] Jameson, A., "Iterative Solution of Transonic Flow over Airfoils and Wings, Including Flows at Mach 1," *Communications on Pure and Applied Mathematics,* Vol. 27, May 1974, pp. 283-309.

[15] Landrum, E. J., "A Tabulation of Wind Tunnel Pressure Data and Section Aerodynamic Characteristics at Mach Numbers of 1.61 and 2.01 for Two Trapezoidal and Three Delta Wings Having Different Surface Shapes," NASA TN D-1394, Sept. 1962.

[16] Woodward, F., "An Improved Method for the Aerodynamic Analysis of Wing-Body-Tail Configurations in Subsonic and Supersonic Flow," NASA CR 2228, 1973.

[17] Grossman, B. and Siclari, M. J., "The Non-Linear Supersonic Potential Flow over Delta Wings," AIAA Paper 80-0269, Jan. 1980.

[18] Landrum, E. J., "Wind Tunnel Pressure Data at Mach Numbers from 1.6 to 4.63 for a Series of Bodies of Revolution at Angles of Attack from -4 to 60°," NASA TM X-3558, Oct. 1977.

[19] Marconi, F., Salas, M., Yeager, L., "Development of a Computer Code for Calculating the Steady Super/Hypersonic Inviscid Flow Around Real Configurations, Vol. I-Computational Techniques," NASA CR 2675, April 1976.